Densification of quartz powder and reduction of conductivity at 700°C

David Lockner
U.S. Geological Survey, Menlo Park, California

Brian Evans
Department of Earth, Atmospheric and Planetary Sciences, Massachusetts Institute of Technology, Cambridge, Massachusetts

Abstract. We have measured axial strain, volumetric strain, and electrical conductivity during the densification at 700°C of ultra-fine quartz powder (5–10 μm diameter) saturated with distilled water. Individual experiments were run at confining pressures ranging from 200 to 370 MPa and pore pressures of 30, 100, and 200 MPa. During the experiments, which lasted from 10 hours to 8 days, the porosity decreased from an initial value of about 40% to final porosities ranging from 19% to as little as $8 \pm 1\%$. In all experiments, initial volumetric compaction rates were rapid (10^{-5} to 10^{-6} s^{-1}) but decreased to between 10^{-7} and 10^{-8} s^{-1} after approximately 1 day. Electrical conductivity also decreased monotonically from 10^{-2} to 10^{-4} S/m during the experiments. We present a model in which changes in conductivity are controlled by constrictions in interconnecting channels, while porosity is controlled primarily by deposition of quartz in the pores. Both experimental and model results suggest a densification process in which conductivity reduces to matrix conductivity while leaving a residual porosity of 3–5%. In the Earth, the porosity at a given instant will be the net resultant of porosity reducing processes and porosity producing processes including fracturing. The rapid loss of conductivity and, by inference, permeability suggests that in the absence of processes which increase permeability, both of these properties should have very small values in the lower crust. Furthermore, these experiments lend support to arguments that time-dependent compaction of fault gouge can play an important role in modifying fluid pressure and fault strength during the interseismic portion of the earthquake cycle for large earthquakes.

Introduction

Widespread geologic evidence suggests that fluid pressures are sometimes elevated over a large fraction of Earth's crust, and syntectonic hydrofracture events may be relatively common [*Fyfe et al.*, 1978; *Etheridge et al.*, 1984; *Walder and Nur*, 1984], perhaps at all metamorphic grades [*Ross and Lewis*, 1989]. High pore fluid pressure might also explain the apparent weakness of the San Andreas fault [*Byerlee*, 1990, 1993; *Rice*, 1992]. Recent friction experiments [*Blanpied et al.*, 1992] provide another example of the interplay between elevated pore fluid pressure, permeability, and rock strength. In contrast, other observations require the presence of connected porosity and substantial flow of fluids at depth [e.g., *Sibson*, 1981; *Walder and Nur*, 1984; *Nur and Walder*, 1992]. However, if high pore pressures along faults are to be maintained over geologic time, either rock permeability must be rather low, of the order of 1 ndarcy (10^{-21} m^2) [*Bredehoeft and Hanshaw*, 1968; *Nur and Walder*, 1992] or there must be an active source of overpressured fluids at depth [*Rice*, 1992]. The two sets of observations may be reconciled if permeability is regarded as a dynamic property. Thus a quantitative knowledge of the rate of change of transport properties of rocks under various conditions of effective stress, temperature, and pore fluid chemistry is critical to understanding tectonic processes [*Gueguen et al.*, 1986; *Byerlee*, 1990; *Nur and Walder*, 1992; *Rice*, 1992; *Byerlee*, 1993; *Moore et al.*, 1994].

The way that pore connectivity changes is a particularly important issue. Does the rock porosity remain connected as the pore geometry is changed by cementation, deformation, solution transfer processes, or metamorphic reactions? How is pore geometry altered under hydrostatic and nonhydrostatic stress states? If the pore structure remains connected, water released during prograde metamorphism will be able to migrate at

Paper number 94JB02818.
0148-0227/95/94JB-02818$05.00

relatively low fluid pressures. On the other hand, if pores tend to become isolated, fluid pressures could rise nearly to lithostatic values.

The properties of rocks in the lower crust are inferred primarily through remote sensing techniques based on measurements of seismic wave velocities and attenuation, gravity, and electrical conductivity; all are properties that depend critically on pore connectivity. Conductivity is particularly sensitive. In Earth's crust, the dominant mineral phases are poor conductors, and resistivity is determined primarily by the movement of ions dissolved in the pore fluids [*Olhoeft*, 1981]. Here we report progress on experiments which illustrate the interrelationship of pore geometry, solution transfer processes, and electrical conductivity. Many questions remain, but the compaction rate and conductivity data are unique and of interest in their own right.

Technique

The starting material for all experiments was ultrafine quartz powder obtained by classifying crushed Ottawa sand in an air centrifuge. The average spherical grain size of the powder was about 5–10 μm (Figure 1). In one experiment, we used a second powder fraction which had average grain size of about 20 μm. Before loading into the hot isostatic press (HIP) assembly, the powders were compacted at room temperature in a steel die with an axial stress of 300 ± 60 MPa; the porosity of these starting samples was 0.46 ± 0.02 for the finer powder and 0.41 for the powder with the larger grain size. The precompacted samples were 19.1 mm in diameter and about 18 mm long. In one experiment (experiment 12), uncompacted powder was used.

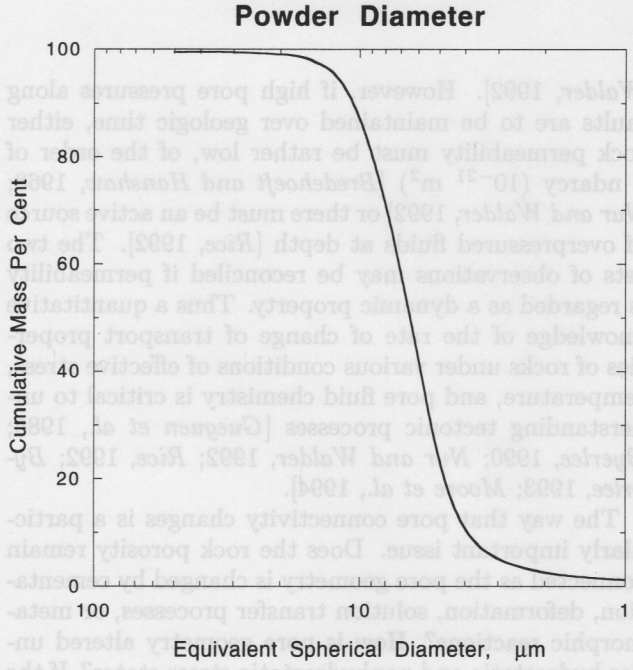

Figure 1. Powder curve, percent finer than versus grain size.

These cold-pressed samples were sandwiched between aluminum oxide spacers in a silver-plated copper jacket about 0.51 mm thick, which acted as one of the electrodes for measuring conductivity (Figure 2). Distilled, deionized water had access to the sample through axial holes in the spacers, which also contained a thermocouple. A ceramic frit, made of 99% Al_2O_3 bonded by boro-silicate glass (Coors AH99), was placed between the sample and the pore fluid port. The frit had a porosity of 28% and allowed the pore fluid to communicate with the sample but prevented the powder from extrud-

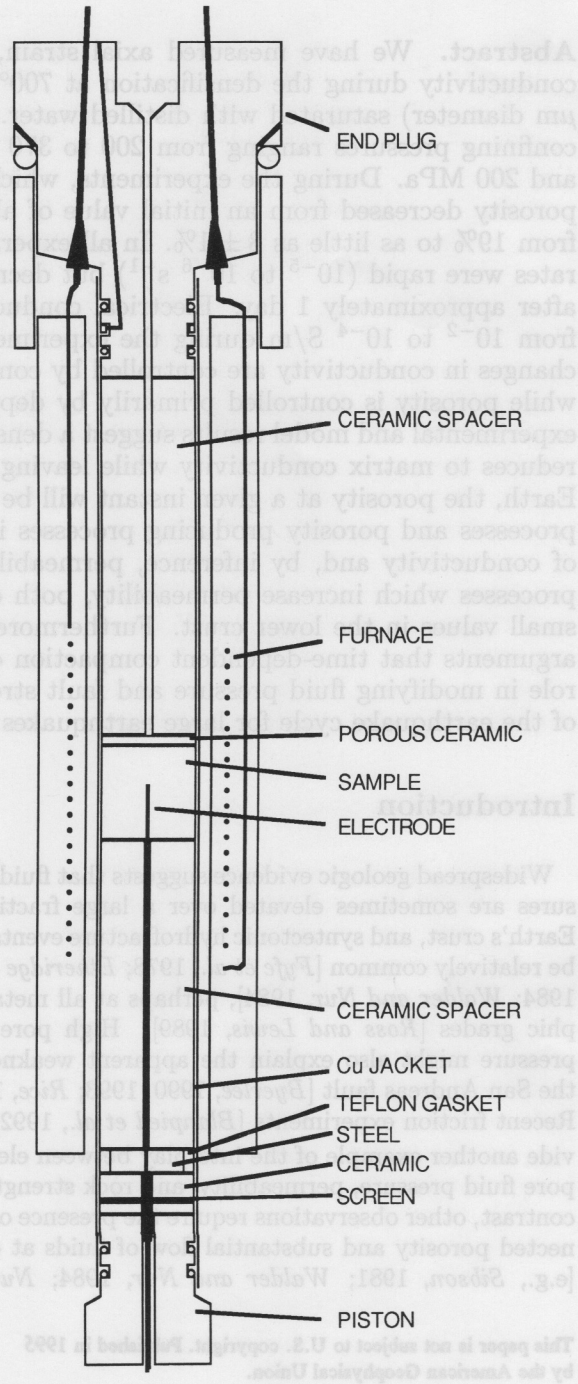

Figure 2. Sample column assembly for hot press experiments.

Table 1. Run Conditions

Run	Grain Size, μm	P_c, MPa	P_p, MPa	P_e, MPa	Ending ϕ ($\pm$0.01)	m (Archie's Law)
9	5–10	200	30	170	0.18	
10	5–10	200	30	170	0.19	3.6
11	>20	200	30	170	0.10	0.9
12	5–10	370	30	340	0.08	2.1
13	5–10	370	200	170	0.07($\pm$0.02)	3.0
14	5–10	270	100	170	0.11	1.9
15	5–10	270	100	170*	0.11	1.7

All runs at 700°C.
*Run 15 was precompacted at $P_c = 370$ MPa, $P_p = 0, T = 18$°C.

ing up the thermocouple hole. A central silver electrode, 1.9 mm in diameter, was inserted through the lower alumina spacers and penetrated about 10.0 ± 0.05 mm into the sample.

The experiments were intended to run for several days, so it was critical that the sample and the pore fluid system were strictly isolated from the argon-confining medium. Thus we constructed a special assembly consisting of two viton o-rings and an intermediate split steel ring which was vented to the atmosphere (Figure 2). Any gas which leaked past the upper o-ring was trapped by the split-ring assembly. Because of the positive pore pressure in the sample, argon cannot enter the pore fluid system. Similar isolation is achieved in the lower seal assembly by placing a stainless-steel screen at the top of the piston, which allows the argon to escape through the hole in the lower piston.

The completed sample assembly was surrounded by a Pt-wire resistance heater, packed with boron nitride, and loaded into an internally heated, gas-medium, deformation apparatus. The sample assembly was pressurized to confining pressures of 200 to 370 MPa and pore fluid pressures of 30, 100, or 200 MPa (Table 1). The temperature was then raised to 700°C while the confining and pore fluid pressures were held constant by an automated control system. At the run conditions, β-quartz was the stable phase. Confining and pore fluid pressures were measured with a manganin cell and a strain-gauge pressure transducer, respectively.

The volume of the sample was measured during the experiment in two ways. First, the sample was touched by the bottom piston, which was advanced by a high-speed servo-control system, set to maintain axial stress equal to the confining pressure. A DCDT displacement transducer, attached to the piston, provided a continuous record of axial shortening dl. The volumetric strain ε_v was computed from axial strain $\varepsilon_a = dl/l_o$, assuming isotropic compaction (i.e., $\varepsilon_v = (1 + \varepsilon_a)^3 - 1$). A second independent measure of volumetric strain was obtained by measuring the volume of pore fluid needed to maintain constant fluid pressure. Provided that the porosity remains completely connected, the measured volume represents the volume lost by the sample [see *Morrow et al.*, 1994; *Zhang et al.*, 1994]. The pore volume system could resolve changes of 0.015 mm^3, or approximately $\partial\varepsilon_v = 3$ μstrain.

Pressures, temperature, and displacement were recorded automatically once every second using a 16-bit multiplexed A/D converter. Accuracies of confining pressure, P_c, and pore fluid pressure, P_p, were 1.0 and 0.5 MPa, respectively; precisions were 0.2 MPa. Precision of the axial displacement was 0.3 μm. The samples were under nearly hydrostatic loading, except near the junction with the alumina spacers. Here friction between the sample and the alumina causes the densification to proceed more slowly than in the remainder of the sample. The final density was computed from the measured sample dimensions, the starting weight, and an assumed density of 2.65 g/cm^3 for quartz. Because of the uneven densification near the alumina pieces, the final density is uncertain by approximately 1%. The porosity at any given time was determined from the instantaneous axial shortening data and the final porosity. Consequently, instantaneous porosity values have greater uncertainties during the early stage of the experiments. The temperature at the ends of the samples was lower than the center by about 15°C.

The sample resistance was measured periodically by comparison to a precision decade resistor connected in series (Figure 3). A signal generator provided a 100-

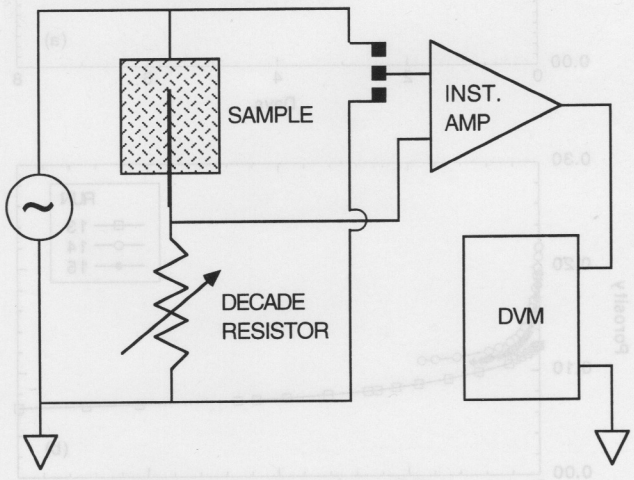

Figure 3. Schematic diagram of sample resistance measurement circuit. Voltage drop across sample is balanced against voltage drop across precision decade resistor. Excitation is 1 Vp–p at 100 Hz.

Hz sine wave excitation signal of 1 V, peak-to-peak. A high-input-impedance amplifier ($> 3 \times 10^8\ \Omega$) was then connected alternately across the sample and across the resistor box. The resistors were adjusted until the voltage drop equaled that of the sample. Sample resistances ranged from 10^3 to $10^6\ \Omega$. Although the sample resistance was determined to $\pm 0.5\%$ accuracy, conversion to conductivity, σ, requires a scaling factor, α, such that $\sigma = 1/\alpha R$. This factor depends on the sample geometry and therefore changes as densification proceeds. A radially symmetric finite difference model was developed to compute α. For the nominal sample dimensions, $\alpha = 0.027 \pm 0.005$ m. No correction was made in the conductivity data for the gradual increase in α that occurred as each sample compacted and reduced the jacket-central electrode spacing. This systematically increasing error in conductivity is no more than 6%.

Results

Run conditions, starting materials, and ending porosities for the experiments are listed in Table 1. Densification and conductivity curves are shown in Figures 4–6. In most experiments, the effective pressure, $P_e = P_c - P_p$, was 170 MPa. The compaction histories of all runs are similar and involve an initial period of rapid compaction, followed by much slower rates after approximately 10 hours (Figure 4). The fastest initial

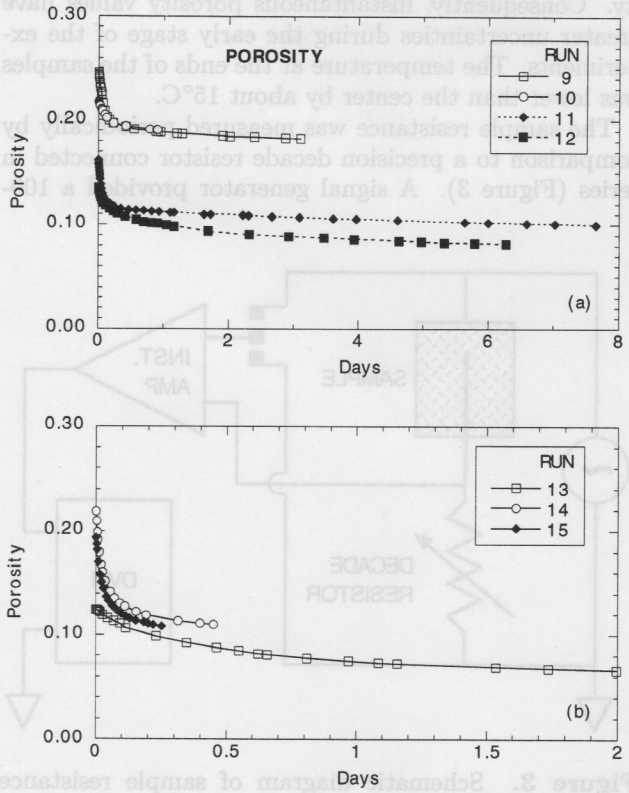

Figure 4. Density versus time from axial displacement data. (a) Runs 9–12. (b) Runs 13–15.

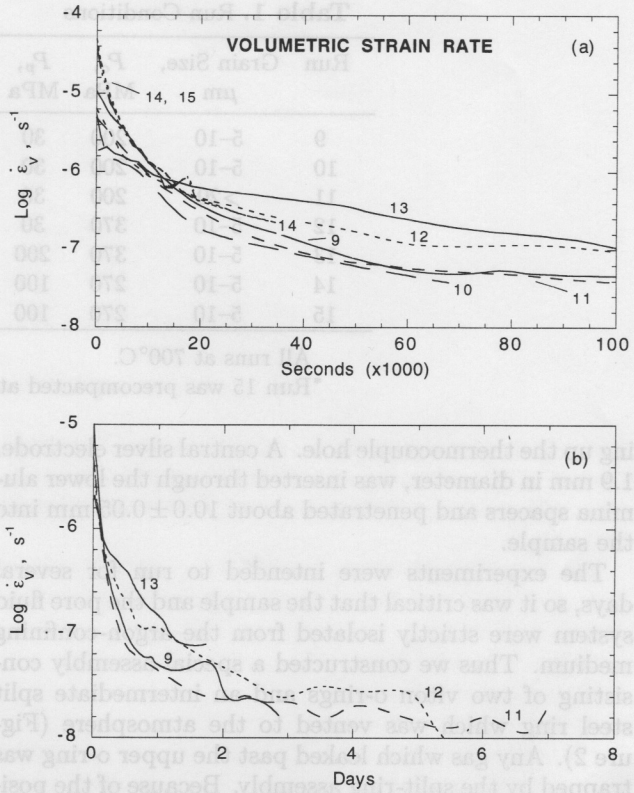

Figure 5. The $\log_{10} \dot{\varepsilon}_v$ versus time from axial displacement data.

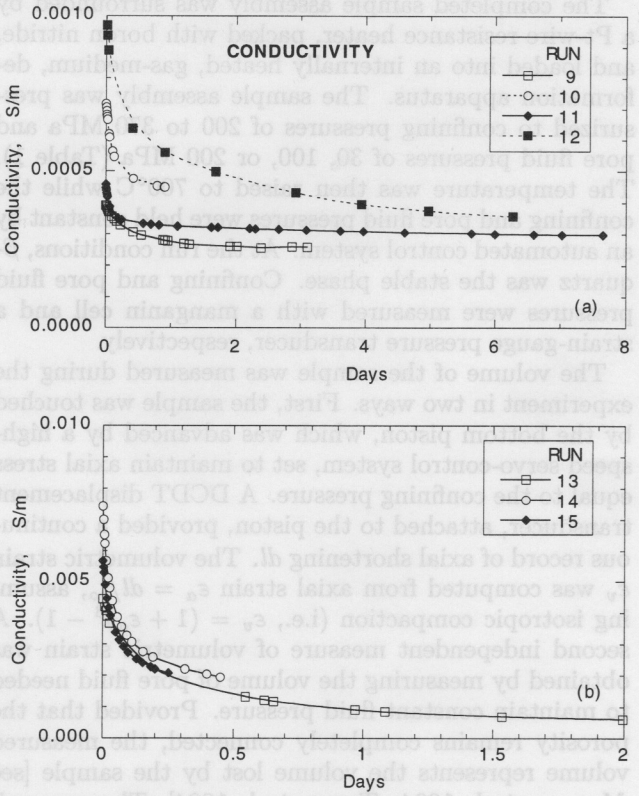

Figure 6. Conductivity versus time. (a) Runs 9–12. (b) Runs 13–15.

compaction rates shown are for experiments 14 and 15 where $P_p = 100$ MPa, but run 13 ($P_p = 200$ MPa) actually had the fastest compaction rate. However, due to equipment problems, this sample had to be unloaded and restarted, and consequently, the initial rate is not shown. After 2 days, compaction rates for the runs at $P_p = 30$ MPa had decayed to approximately $2 - 3 \times 10^{-8}$ s^{-1} (i.e., about 0.2% porosity loss per day). Thus little additional porosity loss can be expected for reasonably lengthed experiments. However, notice that the 200 MPa pore pressure run (experiment 13) was compacting 4 to 5 times faster, possibly owing to increased H_2O activity at high pore pressure. Densification of porous quartz aggregates has been studied by several workers [e.g., *Sprunt and Nur*, 1977a, b; *den Brok and Spiers*, 1991; *Cox and Paterson*, 1991; *Schutjens*, 1991]. We defer a detailed analysis of the densification process in our experiments to a later time and instead focus here on the relationship between densification and conductivity reduction.

In some experiments we also measured the volume of pore fluid removed from the sample by adjusting the volume of the reservoir at room temperature to maintain constant pore pressure. These data provide an independent measure of sample compaction to test the accuracy of the determination of porosity from axial shortening. Data from run 15 at $P_p = 100$ MPa are shown in Figure 7, where the change in volume of the pore pressure intensifier is plotted as a function of porosity calculated from axial shortening data. Since fluid mass is conserved in the pore fluid system, the volume change in the sample can be related to the volume change in the intensifier by

$$V_2 = \frac{\rho_1}{\rho_2} V_1 \qquad (1)$$

where ρ_1 is density of water in the pressure intensifier at room temperature and ρ_2 is density of water in the sample at 700°C. A least squares fit to the data requires a density ratio of 3.2 ± 0.2. The correct ratio of 3.55 is represented by the slope of the line shown in Figure 7. Note that by the end of the experiment (porosity ranging from 0.10 to 0.14) the data do fall along a line with the correct slope. One possible cause of the discrepancy in the early stage of the experiment could be anisotropic sample compaction due to the strength of the copper jacket and silver electrode. For example, the two pore volume determinations shown in Figure 7 could be reconciled if radial strain were 16% more than axial strain. Since porosities are back-calculated from the ending sample dimensions, beginning porosities are systematically calculated too small. For example, in run 15, a back-calculated porosity of 18% should in fact be 19.5% based on the amount of water expelled from the sample. Pore volume measurement was made for only a few of the runs, and so we did not correct any other data.

Conductivity decreases monotonically as porosity decreases (Figure 8). For a given porosity, conductivity tends to increase with increasing pore pressure. Since fluid density increases with pressure, one also expects fluid conductivity to increase. The conductivity data of run 12 is apparently anomalous, since it has lower porosity than runs 9 and 10 but has about the same conductivity. It was, however, the only sample run at high effective pressure (370 MPa), but, in addition, it was not cold pressed as were all other samples. Possibly, the high conductivity of this sample reflects an unusually loose grain-packing geometry. This conjecture needs to be verified by additional experiments. Another notable feature of Figure 8 is the shallow slope and relatively high conductivity of run 11 (compared to runs 9 and 10). This sample was the one made from the unsorted >20 μm powder. Here again, changes in grain packing geometry are possible.

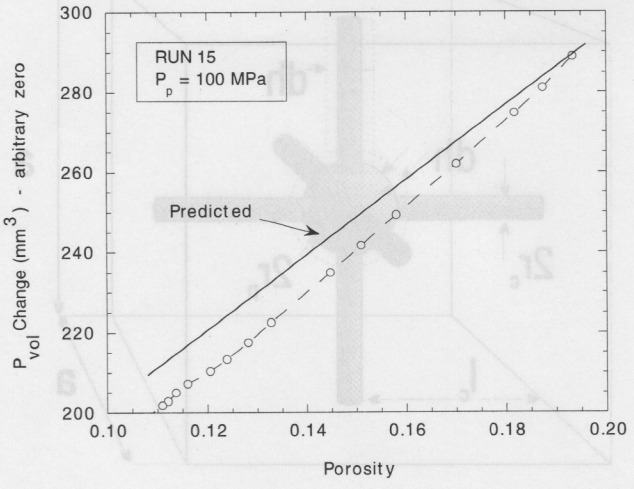

Figure 7. Plot of porosity change as calculated from axial shortening versus pore fluid removed from sample to maintain constant pressure. Solid line shows expected slope based on density contrast of water at room temperature and 700°C.

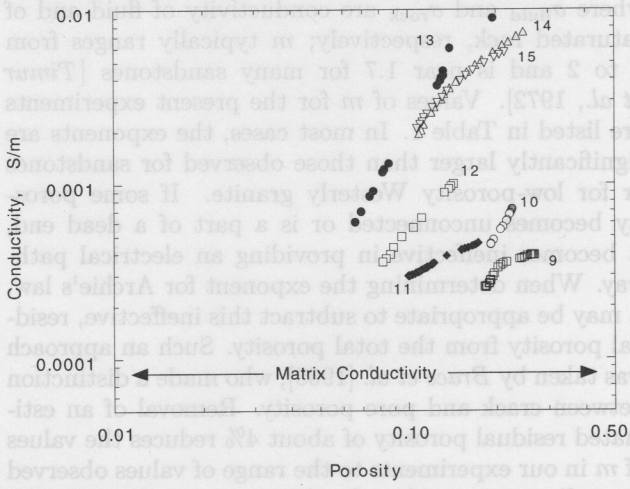

Figure 8. The log σ versus log ϕ for all experiments. Matrix conductivity was determined from evacuated sample. See Table 1 for values of exponent in power law fit.

The matrix conductivity was determined to be 8×10^{-5} S/m by measuring a sample (run 10) which was loaded mechanically and at temperature, but with no fluid present. Conductivity for single-crystal quartz is highly anisotropic [*Kronenberg and Kirby*, 1987]. Conductivity perpendicular to the c axis is approximately 10^{-5} S/m at 700°C, but parallel to c, conductivities as high as 10^{-2} have been reported. Values that we have measured for the dry aggregate are approximately one-half the conductivity reported by *Olhoeft* [1981] for dry Westerly granite and a hornblende schist at the same temperature. The lower conductivity of the dry quartz powder is probably due to inefficient conduction paths through the relatively narrow grain contacts since dry pores will be nonconducting. One of the primary reasons for undertaking the experiments on water-saturated quartz aggregates was to determine whether the pores remained connected as the samples compacted. If interconnecting fluid-filled passages pinch off so that pores become isolated, then the sample conductivity should drop to the value for matrix conduction at some residual porosity. But, if pores remained connected, matrix conductivity should be reached as porosity approaches zero. As shown in Figure 8, we have come within one-half decade of the matrix conductivity without observing a discontinuity in slope, indicating that in the experiments performed so far, channels shrink but remain interconnected.

Discussion and Model Development

Archie's law is a well-known empirical relation between conductivity and porosity which is used mainly for sedimentary rocks [*Timur et al.*, 1972] but which has also been applied to crystalline rocks [e.g., *Brace et al.*, 1965; *Lockner and Byerlee*, 1986]. The most common form of Archie's law is

$$\frac{\sigma_{\text{fluid}}}{\sigma_{\text{rock}}} = \phi^{-m} \qquad (2)$$

where σ_{fluid} and σ_{rock} are conductivity of fluid and of saturated rock, respectively; m typically ranges from 1 to 2 and is near 1.7 for many sandstones [*Timur et al.*, 1972]. Values of m for the present experiments are listed in Table 1. In most cases, the exponents are significantly larger than those observed for sandstones or for low-porosity Westerly granite. If some porosity becomes unconnected or is a part of a dead end, it becomes ineffective in providing an electrical pathway. When determining the exponent for Archie's law, it may be appropriate to subtract this ineffective, residual porosity from the total porosity. Such an approach was taken by *Brace et al.* [1965], who made a distinction between crack and pore porosity. Removal of an estimated residual porosity of about 4% reduces the values of m in our experiments to the range of values observed for sedimentary rocks. In this sense, uncharacteristically large values of m may be indicative of rocks in which a significant residual porosity has become nearly isolated.

Conductivity-Porosity Model

Pore geometry and therefore transport pathways can be very complex. A variety of approaches have been used to construct simplified, numerically tractable models that are able to describe the important geometrical features controlling transport properties. For example, permeability and conductivity have been analyzed using an equivalent channel model that replaces the true porosity with idealized, simple channels whose transport properties can be calculated [*Paterson*, 1983; *Walsh and Brace*, 1984; *Lockner et al.*, 1991; *Morrow et al.*, 1994]. Changes in permeability accompanying porosity reduction have also been analyzed using percolation theory, network models, and stochastic sampling procedures [*Schwartz and Banavar*, 1989; *Schwartz et al.*, 1989; *Germanovich and Lowell*, 1992; *David et al.*, 1994; *Lowell et al.*, 1993; *Zhu et al.*, 1995].

We model our conductivity data by considering geometric changes in the pore structure during densification and developing what is essentially an equivalent channel (or unit cell) model. The following assumptions are used:

1. A representative unit cell with length a is characterized in terms of its final or residual porosity ϕ_r and connecting channel ways. Each unit cell contains a single spherical pore connected to neighboring pores by z channels (Figure 9). Asymptotes in the conductivity data (Figures 4 and 8) indicate that ϕ_r lies between 0 and 6% .

2. All current paths are from pores (high σ) through connecting channels (low σ) to neighboring pores. The connecting channels are expected to dominate conductivity, especially as channels close.

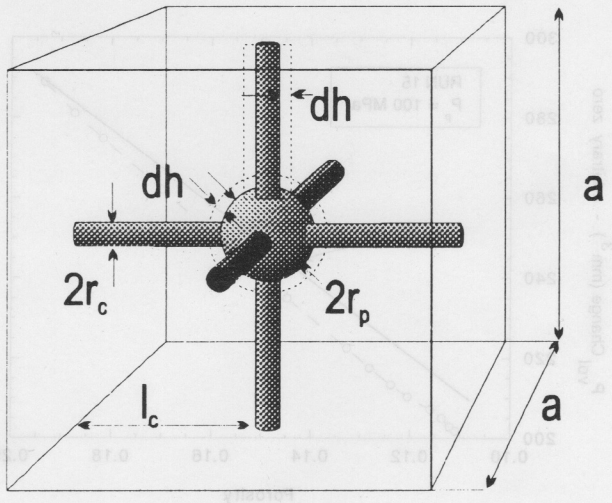

Figure 9. Cut-away view of unit cell in densification model. Porosity loss is assumed to result from dissolution of quartz at high-stress grain contacts. This dissolved quartz is then deposited uniformly along walls of pores and channel ways.

3. Porosity loss is assumed to occur through redistribution of quartz within each unit cell (matrix mass is conserved). The dominant mass transport mechanism is dissolution of quartz at grain contacts and redeposition along walls of channels and pores. Thus the unit cell dimension decreases monotonically as pore water is expelled and/or compressed.

4. Incremental thicknesses of quartz deposited on channel and pore walls are represented by dh_c and dh_p, respectively. As a starting model, we assume that for each time increment the change in wall thickness is the same in channels and in pores: $dh_c = dh_p = dh$.

5. Cross sections of channels and pores are assumed to be approximately circular and are represented by equivalent radii r_c and r_p.

6. Unit cell dimension decreases during densification. In the final state ($a = a_r, \phi = \phi_r$), pore volume dominates resulting in the conditions: $\phi_c \ll \phi_p \cong \phi_r$ and $r_c \cong 0$. Therefore, by integrating the relationships in assumption (4), we have $r_c = h$ and $r_p = h + r_{pr}$ where r_{pr} is the residual pore radius.

We use an underscore to denote nondimensional parameters normalized by the final state unit cell length a_r (e.g., $\underline{r}_p = r_p/a_r; \underline{V}_T = \underline{a}^3 = (a/a_r)^3$). Assumption 4 allows us to parameterize the densification history in terms of h and, given the final conditions (assumption 6), to back-calculate pore geometry at all earlier times. From the pore geometry we then calculate unit cell conductivity. The coordination number for the pores, z, is related to grain packing. Since we assume a single representative pore size, effects due to grain size distribution, angularity, and channel tortuosity are neglected. These effects may, to some degree, be incorporated in the value chosen for z. Furthermore, while z may evolve in the real samples during densification, we will, for now, consider it to be constant. We begin by modeling the well-sorted (5–10 μm) quartz powder. Hexagonal close-packed spheres of equal size would produce a starting porosity of $\phi \sim 0.26$. From the density determinations ($\phi = 0.46 \pm 0.02$) of the cold press procedure, we know that the starting samples actually have a less efficiently packed structure. SEM studies show that the initial powder grains are very angular and aspherical, but the sharp corners are reactive, and grains rapidly become rounded during the experiment. Thus it is not clear how severe the errors introduced by the idealized unit cell model are.

Parameterization of Pore Reduction

In this section we derive an expression for the channel and pore volumes in terms of the growth parameter $\underline{h}$. Referring to Figure 9, the relative volumes are

Pore volume $$\underline{V}_p = \tfrac{4}{3}\,\pi\,\underline{r}_p{}^3 \tag{3a}$$

Channel volume $$\underline{V}_c = \pi\,\underline{r}_c{}^2\underline{l}_c \tag{3b}$$

Total porosity $$\underline{V}_\phi = \underline{V}_p + z\,\underline{V}_c \tag{3c}$$

Matrix volume $$\underline{V}_m = (1 - \phi_r) \tag{3d}$$

Unit cell volume $$\underline{V}_T = \underline{a}^3 = \underline{V}_m + \underline{V}_\phi \tag{3e}$$

and, by definition

$$\underline{V}_\phi = \phi \underline{V}_T\,. \tag{3f}$$

Combining (3d), (3e), and (3f) gives

$$\underline{V}_\phi = \phi \frac{(1 - \phi_r)}{(1 - \phi)}\,. \tag{4}$$

Next, from assumptions 4 and 6 we have

$$\underline{r}_p = \underline{r}_{pr} + \underline{h} \tag{5a}$$

$$\underline{r}_c = \underline{h} \tag{5b}$$

$$\underline{a} \approx 2(\underline{l}_c + \underline{r}_p)\,. \tag{5c}$$

In (5a), $\underline{r}_{pr}$ is the final pore radius. Equation (5c) is used to express $\underline{l}_c$ in terms of known parameters. Substituting (5) into (4) and using definitions (3a) and (3b) results in a cubic equation expressing $\underline{h}$ in terms of ϕ, ϕ_r and z:

$$C_3\underline{h}^3 + C_2\underline{h}^2 + C_1\underline{h} + C_0 = 0 \tag{6a}$$

where

$$C_0 = \frac{1}{\pi}\frac{(\phi_r - \phi)}{(1 - \phi)} \tag{6b}$$

$$C_1 = \left(\frac{6\phi_r}{\pi}\right)^{2/3} \tag{6c}$$

$$C_2 = (4 - z)\left(\frac{3\phi_r}{4\pi}\right)^{1/3} + \frac{z}{2}\left(\frac{1 - \phi_r}{1 - \phi}\right)^{1/3} \tag{6d}$$

$$C_3 = \frac{4}{3} - z\,. \tag{6e}$$

Unit Cell Conductivity

Through equation (6) we can relate porosity to the change in channel and pore dimensions. The next step is to relate unit cell conductivity to $\underline{h}$. This is an easy matter for individual channel ways. For parallel current flow, conductivity is expressed as $\sigma = Y(\text{length/area})$ where Y is admittance. Thus, for an individual channel (Figure 9) we have

$$Y_c = \sigma_{\text{fluid}}\frac{a_r^2\pi\underline{r}_c^2}{a_r\underline{l}_c} = \sigma_{\text{fluid}}a_r\frac{\pi\underline{h}^2}{\left(\frac{a}{2} - \underline{r}_{pr} - \underline{h}\right)}\,. \tag{7}$$

Since channel cross sections become vanishingly small in this model as the residual porosity is approached, we have from (7) that $Y_c \to 0$ as $\phi \to \phi_r$.

Pore admittance is more difficult to calculate, but as we will show, it has a secondary effect on total conductivity for the range of porosities measured in the experiments. Consequently, for current flow traveling across the pores, we will approximate the length of the flow path as $\sim 2a_r\underline{r}_p = 2a_r(\underline{r}_{pr} + \underline{h})$ and the average cross-sectional area of the flow path as $\sim\pi(a_r\underline{r}_p)^2 = \pi a_r{}^2(\underline{r}_{pr} + \underline{h})^2$. These approximations result in a pore admittance of

$$Y_p = \sigma_{\text{fluid}}a_r\frac{\pi(\underline{r}_{pr} + \underline{h})}{2}\,. \tag{8}$$

Finally, we note that in the model, current flow must travel through each unit cell by channel-pore-channel paths. For uniform flow in a three-dimensional connectivity network, an average of $z/6$ channels are available to conduct current from the cell edge to the pore. Unit cell admittance can therefore be expressed as

$$\frac{1}{Y_{uc}} = \left(\frac{6}{z}\right)\frac{1}{Y_c} + \frac{1}{Y_p} + \left(\frac{6}{z}\right)\frac{1}{Y_c} = \frac{1}{Y_p} + \left(\frac{12}{z}\right)\frac{1}{Y_c} \; . \quad (9)$$

Conductivity of the unit cell, and therefore of the entire matrix, becomes

$$\sigma = Y_{uc}\frac{a}{a^2} = \frac{Y_{uc}}{(a_r \underline{a})} \; . \quad (10a)$$

Substituting (8) and (9) gives

$$\sigma = \sigma_{\text{fluid}}\frac{\pi}{\underline{a}}\left[\frac{2}{(\underline{r}_{pr} + \underline{h})} + \frac{12}{z}\frac{\left(\frac{\underline{a}}{2} - \underline{r}_{pr} - \underline{h}\right)}{\underline{h}^2}\right]^{-1} \; . \quad (10b)$$

As expected, sample conductivity is proportional to fluid conductivity. Furthermore, conductivity does not scale with grain size (approximately the unit cell dimension a_r) but depends only on nondimensional length parameters such as $\underline{a}, \underline{r}_{pr}$, and $\underline{h}$. This is the result of an implicit assumption that the boundary layer for ionic transport is small relative to the cross section of pores and channels.

Figure 10 shows a representative plot of $\log \sigma$ versus $\log \phi$ for parameter values of $\phi_r = 4\%$ and $z = 6$. For porosity less than 30%, conductivity of pores exceeds channel conductivity. Since these conductivities are added in series to produce the total sample conductivity, channel ways limit the current over the entire range of porosity. For ϕ greater than about 15%, pore conductivity reduces σ_{rock} by a minor but increasing amount. Although this is a relatively small effect, it is sufficient to limit the slope for $\log \sigma_{\text{rock}}$ to a nearly constant value of 1.79. This slope is equivalent to the exponent m in Archie's law (equation (1)) and is remarkably close to values observed for sandstones [*Timur et al.*, 1972]. The fit appears to be more than coincidental and may provide the basis for a physical mechanism to explain Archie's law. The other feature built into the model is the roll off in $\log \sigma$ as the limiting value of $\log \phi_r$ is approached. This is a key feature which we describe in greater detail in the next section.

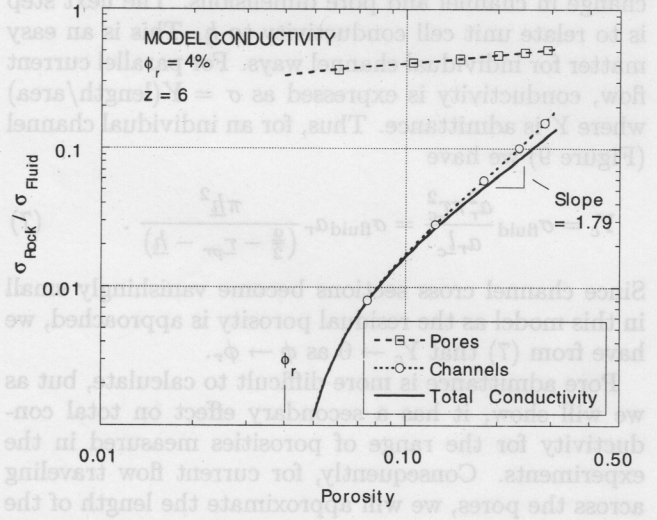

Figure 10. $\log \sigma$ versus $\log \phi$ for model with residual porosity of 4% and 6 connecting channels per unit cell. Channel conductivity is less than pore conductivity for all porosities and therefore limits total conductivity. For porosity >15%, power law exponent is 1.79 and is in good agreement with Archie's law values for porous sandstones.

Comparison of Experimental and Model Results

Equation (10) will generate a family of curves depending on the choice of ϕ_r. Since these curves all exhibit a gradual change in slope, fitting the individual data segments from the various runs is a severely underdetermined problem. If we assume that the suite of runs, using the same starting material and conducted at the same effective pressure and temperature, all represent portions of a single densification curve, we can construct a master compaction curve by shifting conductivity data from the various runs vertically so that they overlap. Such a composite curve, using data from runs 9, 10, 12, 13, 14, and 15, is presented in Figure 11. Where the various data sets overlap in Figure 11, their slopes are in general agreement with each other, providing some confidence that this procedure is valid. The relative shifts in the data sets are assumed to be the result of variations in fluid conductivity. Fluid conductivities, normalized by run 13, are predicted to be 0.04, 0.06, 0.7, and 0.7 for runs 9, 10, 14, and 15, respectively.

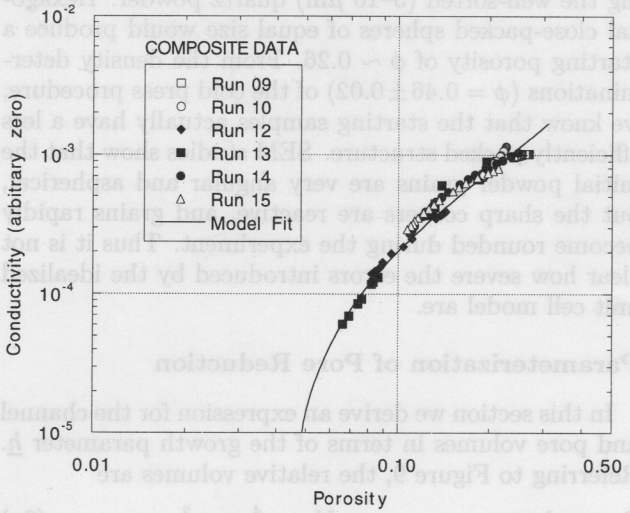

Figure 11. Composite conductivity curve for all runs in which $P_e = 170$ MPa. Data sets are shifted vertically to overlap. Model curve from Figure 10 is reproduced for comparison and suggests that densification of quartz samples is proceeding toward a residual porosity of approximately 4%.

Since runs 9 and 10 had the same run conditions, a discrepancy in their fluid conductivities probably indicates a problem in one or both of these runs. Experiment 10 had been run dry at temperature to measure matrix conductivity. It was then cooled, saturated and reheated. Consequently, it may have suffered damage due to thermal cracking, providing a possible explanation for its enhanced conductivity. In addition to the experimental results, the analytical model curve is also plotted in Figure 11 (shifted vertically to match the data) using $\phi_r = 4\%$ and $z = 6$.

In an earlier analysis of these data [*Lockner*, 1990] we assumed a cross-over porosity of about 15% above which conductivity was dominated by pore conduction. In the present model, however, conductivity is controlled by current flow in channel ways over the entire range of porosity. This model is more appealing since connecting channels should always be much more resistive than pores. A consequence of this model is an apparent cross-over porosity at about 10%. *Zhu et al.* [1995] have interpreted this break in slope as indicating the approach of a percolation threshold in the pore connectivity. They suggest that at higher porosities, conductivity (and permeability) are controlled by the closing down of the connecting passage ways within the rock. At porosities close to the percolation threshold (equivalent to ϕ_r), more and more passage ways are pinched off, eliminating flow paths within the rock. In our model, however, connecting channels are closed down uniformly, and the entire pore structure remains connected until ϕ_r is reached. Currently available permeability and conductivity data cannot be used to distinguish between these two models. It may be possible, however, by using an oscillatory technique for measuring permeability [*Fischer*, 1992; *Zhang et al.*, 1994] to distinguish between the two models by observing whether total porosity remains connected below the cross-over porosity or whether a divergence between total porosity and connected porosity occurs.

Our model assumptions should be reexamined at this point in terms of how strongly they control the model response. Assumption 1 basically states that conductivity-porosity interaction in the sample can be described in terms of average properties which are represented by a characteristic unit cell. Given the distribution of starting grain sizes (Figure 1) and the angularity of grains, there will clearly be a distribution of pore sizes and connecting channels in the sample. At this point we cannot assess the full implications of this important simplifying assumption. Others have used a similar approach for analysis of permeability-porosity relationships [*Paterson*, 1983; *Walsh and Brace*, 1984; *Lockner et al.*, 1991; *Morrow et al.*, 1994] with good results. Assumption 2 that transport is from pore to pore through connecting channels seems satisfactory for the pore structure developed in these granular aggregates, as well as for porous sandstones in general. For large porosities, the connecting channels become short and in the limit look more like orifices connecting pores rather than channels. For the unit cell geometry shown in Figure 9, channel diameter is twice the channel length at $\phi \approx 0.34$ and represents an upper limit to the porosity that can be meaningfully modeled by this analysis.

As we have shown, overall sample conductivity in the model is controlled by conductivity of connecting channels. However, through assumption 4, pores provide the greatest surface area for deposition of quartz and therefore for porosity reduction. Thus, by setting the relative deposition rates in pores versus channels, assumption 4 is largely responsible for determining the shape of the conductivity-porosity plot shown in Figure 10. As a starting model, we have chosen the simple case of constant deposition rate on all surfaces ($\mathrm{d}h_c = \mathrm{d}h_p = \mathrm{d}h$). While this assumption allows us to develop an analytic expression relating conductivity and porosity, it needs to be refined. It is well known that reduction of surface energy can provide a significant driving force for dissolution-precipitation reactions. Thus rounding of grains and preferential loss of the smallest grains are driven by the tendency to reduce the high surface energy associated with a small radius of curvature of the grain-fluid interface. This driving force can affect the relative deposition rates in pores versus channels. An additional effect is the length of the diffusion path from the source of material at highly stressed grain contacts and regions of small radius of curvature to the pore or channel walls. Proper modeling of these effects is beyond the scope of the present analysis.

Finally, we model the densification process as occurring in a closed system (assumption 6) in which there is no net loss of silica from the sample and quartz is simply transported from grain contacts to neighboring pore or channel walls. Given the rapid densification rates and the constant pore pressure maintained in these experiments, this seems the appropriate boundary condition to apply. If, for example, a large volume of fluid were flushed through the rock during a metamorphic episode, different boundary conditions would be appropriate.

The main features of our model, namely the power law relation of conductivity with porosity at large porosities and the roll-off in conductivity at low porosities. In reality, these features have a rather simple explanation. They are the result of plotting conductivity as a function of total porosity, rather than channel porosity which probably controls the bulk conductivity. As an example, in Figure 12 we have plotted the simple power law relation $\sigma = \phi_c^{1.8}$ not as a function of ϕ_c, but rather as a function of $\phi_{\mathrm{tot}} = \phi_c + c$ where $c = 0.04$. For $\phi_{\mathrm{tot}} \gg c$, a slope of 1.8 is observed. However, near c the slope steepens, and an apparent crossover occurs that is similar to the crossover in Figures 10 and 11. For a function

$$y = (x - c)^r \tag{11}$$

the local slope m on a log–log plot is given by

$$m = \frac{d(\ln y)}{d(\ln x)} = \frac{rx}{x - c}\,. \tag{12}$$

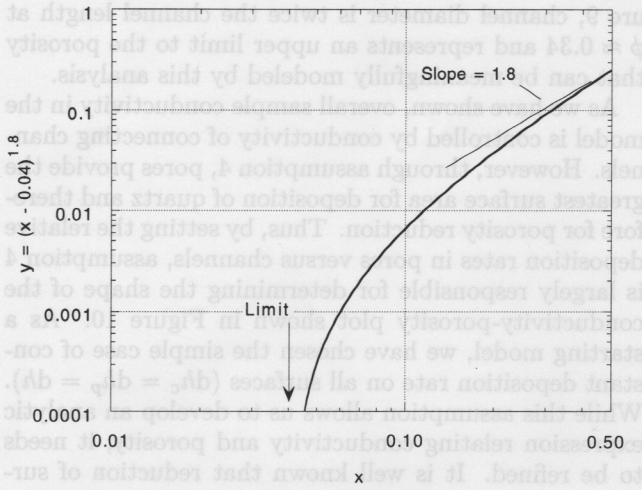

Figure 12. Key features of the densification model are captured by the simple functional form plotted here. If conductivity (or permeability) is controlled by flow in connected channels as is the case in this model, then the inclusion of pore porosity results in an offset in the log-log plot. The result is a break in slope as the residual pore porosity is approached. This feature may be misinterpreted in analyses that do not properly treat residual porosity.

We can determine the value of x where the slope deviates from the asymptotic slope r by an amount ξ by setting $m = (1 + \xi)r$. The solution is

$$x^* = c\left(1 + \frac{1}{\xi}\right) . \tag{13}$$

Using the example plotted in Figure 12, for a break in slope of 50%, we have $x^* = 0.12$. This simple example can be tailored to fit the experimental data remarkably well.

Estimate of Permeability

Using the result in (6), a straightforward estimate of the permeability-porosity dependence can be obtained. To keep this section brief, we consider uniform flow in a medium represented by sixfold coordination of pores ($z = 6$). We compute resistance to flow for channels only, since these dominate fluid transport even more than electrical conductivity. In this case, we apply the Poiseuille formula for flow in a tube [*Brace et al.*, 1968]

$$q = \frac{\pi \Delta P \; R^4}{8 \mu L} \tag{14}$$

where q is flow rate, ΔP is pressure drop, μ is viscosity, R is tube radius, and L is tube length. From Figure 9 we have $R = r_c$ and $L \approx a$. Macroscopic permeability k is expressed by Darcy's law

$$\frac{q}{A} = \frac{k}{\mu} \frac{dP}{dx} \tag{15}$$

where A is cross-sectional area. For the unit cell (Figure 9), $A = a^2$ and $dx = L$. Combining (14) and (15) gives

$$k = \frac{\pi}{8} \frac{R^4}{A} = \frac{\pi}{8} \frac{h^4}{a^2} a_r^2 . \tag{16}$$

Recall that electrical conductivity was independent of grain or pore size (equation (10b)). Because of the strong dependence of flow rate on channel radius, permeability is very sensitive to grain size: $k \propto {a_r}^2$. For $\phi \gg \phi_r$, the model predicts a porosity sensitivity of approximately $k \propto \phi^{3.8}$, although the precise value of the exponent depends on ϕ_r and z. For large porosity, channel diameters become larger than channel lengths, and approximations used to calculate unit cell flow begin to break down. Consequently, the precise value of this limiting exponent predicted by the model may not be so significant. Under these same conditions, permeability often depends on porosity to the third power [*Bernabe*, 1986; *Zhu et al.*, 1995]. A more realistic estimate of channel tortuosity or of the relative deposition rates in pores and channels may correct this discrepancy.

Implications for Crustal Processes

To study processes occurring in the mid to lower crust, it would be desirable to conduct experiments in the 200–400°C temperature range. Instead, we chose to initiate this study at 700°C to drive dissolution-precipitation reactions at a rate that would allow significant compaction within a few days. As long as the same processes are controlling compaction, we expect our results to be applicable at lower temperatures with a trade-off occurring between temperature and strain rate. The initial high compaction rates (Figure 4a) are probably the result of the starting material in these experiments, i.e., angular grains, loose packing (and therefore high grain contact stresses), and undersaturated fluids. Such conditions may actually apply to gouge within a fault zone immediately after an earthquake. This condition is, in fact, a key element in a class of earthquake models currently being developed [*Sleep and Blanpied*, 1992, 1994; *Byerlee*, 1993; *Moore et al.*, 1994; D.A. Lockner and J.D. Byerlee, An earthquake instability model based on faults containing high fluid-pressure compartments, submitted to *Pure Appl. Geophys.*, 1994]. If we assume that densification rate is thermally activated with an apparent activation energy of 80 to 100 kJ/mol (typical of many silicate reactions [*Lockner*, 1993]), then lowering temperature to between 200 and 300°C would reduce the densification rate by 3 to 5 orders of magnitude. These compaction rates would provide significant porosity loss in fault gouge material over the repeat time of large earthquakes (typically measured in hundreds of years), supporting the notion that time-dependent compaction and related pore pressure transients can play an important role in the earthquake cycle.

As the aggregate densifies, its transport properties approach those of a pore-free aggregate. The exact evolution of the porosity will depend on loading conditions, temperature, pressure, chemistry of the pore fluid, and energies of the surfaces and interfaces of the solid phases. If connecting channels are unstable so that pores become isolated, then permeability approaches zero, conductivity approaches matrix conductivity, and fluid in pores is likely compressed to near-lithostatic pressure. If, on the other hand, connecting channels remain stable, they will gradually shrink in diameter as the matrix densifies. Thus, even though pores remain connected, the connecting channels may become so constricted that surface rather than volume conduction will dominate and total conductivity may still approach matrix conductivity. In this case, permeability will also become vanishingly small so that pore fluid pressure will rise nearly to lithostatic levels. In fact, this system is likely to reach a condition in which pore pressure rises, forcing connecting channels open just enough to allow a gradual expulsion of fluid and reduction of pore space (see permeability feedback model discussed by *Rice* [1992]). In both the connected and unconnected models, however, permeability and conductivity are both very low. The exact value of the residual porosity at any given instant probably depends on such factors as the dissolution and precipitation rates of the solid, the mobility of the dissolved solid in the pore fluid, the interfacial and grain boundary energies, the loading conditions and the initial pore geometry. Because the transport properties are largely geometric properties of the pore structure, we suppose that their evolution will also depend on those variables.

In our experiments, conductivity dropped by as much as a factor of 10 to levels that were within one-half decade of the matrix conductivity. Many of the runs appear to be approaching residual porosities of between 3 and 5% at which point total conductivity would be indistinguishable from matrix conductivity. Whether this residual porosity would gradually disappear with further compaction remains an unanswered question. However, it is interesting that independent measurements of wetting angles along the intersections of porosity with grain boundaries in porous quartzite aggregates also suggest that pores will remain connected along grain edges [*Watson and Brenan*, 1987; *Laporte and Watson*, 1991; *Lee et al.*, 1991; *Holness*, 1992]. This appears to be the case even at low porosities, especially if the pore fluid is pure water and low in carbon dioxide content.

Conclusions

Densification rates and electrical conductivity have been measured during hot isostatic pressing of ultrafine quartz powders. Compaction rates were sensitive to P_{H_2O} and to grain size. A conductivity model was developed based on a unit cell concept. The model, which provided a reasonable fit to the data, resulted in conductivity that was controlled by current flow in channel ways at all porosities. Pore conduction had only a minor effect on total conductivity even at 30% porosity. For porosities above about 10%, the model predicts a conductivity-porosity relation in close agreement with Archie's law, although it should be emphasized that other models might also fit the data equally well. In this approach, connecting channel ways shrink uniformly throughout the sample so that all porosity remains connected until residual porosity is reached, in contrast with percolation threshold models in which more and more porosity becomes isolated as the threshold is approached. The general trends observed in these experiments suggest that fault gouge densification following earthquakes can play an important role in changing fluid pressures and fault strength during the interseismic period. Whether porosity remains interconnected or not, fluid-assisted mass transport processes, acting on the grain size scale, will tend to reduce permeability and conductivity in the lower crust to very low values. Fluid pressures might then rise to near lithostatic levels, until new porosity were produced by fracturing or some other process.

Acknowledgments. We thank J. Byerlee, D. Fitterman, A. Nur and T.-f. Wong for their helpful comments and suggestions in reviewing this paper. We gratefully acknowledge support from NSF EAR 61317, the Royal Dutch Shell Petroleum Company and the U.S. Geological Survey National Earthquake Hazards Reduction Program and Deep Continental Studies Program.

References

Bernabe, Y., The effective pressure law for permeability in Chelmsford granite and Barre granite, *Int. J. Rock Mech. Min. Sci. Geomech. Abstr., 23*, 267–275, 1986.

Blanpied, M. L., D. A. Lockner, and J. D. Byerlee, An earthquake mechanism based on rapid sealing of faults, *Nature, 358*, 574–576, 1992.

Brace, W. F., A. S. Orange, and T. R. Madden, The effect of pressure on the electrical resistivity of water-saturated crystalline rocks, *J. Geophys. Res., 70*, 5669–5678, 1965.

Brace, W. F., J. Walsh, and W. Frangos, Permeability of granite under high pressure, *J. Geophys. Res., 73*, 2225–2236, 1968.

Bredehoeft, J. D., and B. B. Hanshaw, On the maintenance of anomalous fluid pressures, I thick sedimentary sequences, *Geol. Soc. Am. Bull., 79*, 1097–1106, 1968.

Byerlee, J. D., Friction, overpressure and fault normal compression, *Geophys. Res. Lett., 17*, 2109–2112, 1990.

Byerlee, J. D., Model for episodic flow of high pressure water in fault zones before earthquakes, *Geology, 21*, 303–306, 1993.

Cox, S. F., and M. S. Paterson, Experimental dissolution-precipitation creep in quartz aggregates at high temperatures, *Geophys. Res. Lett., 18*, 1401–1404, 1991.

David, C., T. F. Wong, W. Zhu, and J. Zhang, Laboratory measurement of compaction-induced permeability change in porous rocks: implications for the generation and maintenance of pore pressure excess in the crust, *Pure Appl. Geophys.*, in press, 1994.

den Brok, S. W. J., and C. J. Spiers, Experimental evidence for water weakening of quartzite by microcracking plus

solution-precipitation creep, *J. Geol. Soc. London, 148*, 541–548, 1991.

Etheridge, M. A., V. J. Wall, S. F. Cox, and R. H. Vernon, High fluid pressures during regional metamorphism and deformation: Implications for mass transport and deformation mechanisms, *J. Geophys. Res., 89*, 4344–4358, 1984.

Fischer, G. J., The determination of permeability and storage capacity: pore pressure oscillation method, in *Fault Mechanics and Transport Properties of Rocks*, edited by B. Evans and T.-F. Wong, pp. 187–211, Academic, San Diego, Calif., 1992.

Fyfe, W. S., N. J. Price, and A. B. Thompson, *Fluids in the Earth's Crust, Dev. Geochem.*, vol. *1*, 383 pp., Elsevier, New York, 1978.

Germanovich, L. N., and R. P. Lowell, Percolation theory, thermoelasticity, and discrete hydrothermal venting in the Earth's crust, *Science, 255*, 1564–1567, 1992.

Gueguen, Y., C. David, and M. Darot, Models and time constants for permeability evolution, *Geophys. Res. Lett., 13*, 460–463, 1986.

Holness, M. B., Equilibrium dihedral angles in the system quartz-carbon dioxide-water-sodium chloride at 800°C and 1-15 kbar: The effects of pressure and fluid composition on the permeability of quartzites, *Earth Planet. Sci. Lett., 114*, 171–184, 1992.

Kronenberg, A. K., and S. H. Kirby, Ionic conductivity of quartz: DC time dependence and transition in charge carriers, *Am. Mineral., 72*, 739–747, 1987.

Laporte, D., and E. B. Watson, Direct observation of near-equilibrium pore geometry in synthetic quartzites at 600–800°C and 2–10.5 kbar, *J. Geol., 99*, 873–878, 1991.

Lee, V., S. J. Mackwell, and S. L. Brantley, The effect of fluid chemistry on wetting textures in novaculite, *J. Geophys. Res., 96*, 10,023–10,037, 1991.

Lockner, D. A., Modeling of brittle failure and comparisons to laboratory experiments, Ph.D. thesis, 218 pp., Mass. Inst. of Technol., Cambridge, 1990.

Lockner, D. A., Room temperature creep in saturated granite, *J. Geophys. Res., 98*, 475–487, 1993.

Lockner, D. A., and J. D. Byerlee, Changes in complex resistivity during creep in granite, *Pure Appl. Geophys., 124*, 659–676, 1986.

Lockner, D. A., S. Hickman, J. D. Byerlee, V. Kuksenko, A. Ponomarev, A. Sidorin, and B. Khakaev, Laboratory-determined permeability of cores from the Kola superdeep well, USSR, *Geophys. Res. Lett., 18*, 881–884, 1991.

Lowell, R. P., P. Van Cappellen, and L. N. Germanovich, Silica precipitation in fractures and the evolution of permeability in hydrothermal upflow zones, *Science, 260*, 192–194, 1993.

Moore, D. E., D. A. Lockner, and J. D. Byerlee, Reduction of permeability in granite at elevated temperatures, *Science, 265*, 1558–1561, 1994.

Morrow, C., D. A. Lockner, S. Hickman, M. Rusanov, and T. Röckel, Effects of lithology and depth on the permeability of core samples from the Kola and KTB drill holes, *J. Geophys. Res., 99*, 7263–7274, 1994.

Nur, A., and J. Walder, Hydraulic pulses in the Earth's crust, in *Fault Mechanics and Transport Properties of Rocks*, edited by B. Evans and T.-f. Wong, pp. 461–474, Academic, San Diego, Calif., 1992.

Olhoeft, G. R., Electrical properties of granite with implications for the lower crust, *J. Geophys. Res., 86*, 931–936, 1981.

Paterson, M. S., The equivalent channel model for permeability and resistivity in fluid saturated rock–A reappraisal, *Mech. Mat., 2*, 345–352, 1983.

Rice, J. R., Fault stress states, pore pressure distributions, and the weakness of the San Andreas fault, in *Fault Mechanics and Transport Properties of Rocks*, edited by B. Evans and T.-f. Wong, pp. 475–503, Academic, San Diego, Calif., 1992.

Ross, J. V., and P. D. Lewis, Brittle-ductile transition: Semi-brittle behavior, *Tectonophysics, 167*, 75–79, 1989.

Schutjens, P. M. T. M., Experimental compaction of quartz sand at low effective stress and temperature conditions, *J. Geol. Soc. London, 148*, 527–539, 1991.

Schwartz, L. M., and J. R. Banavar, Transport properties of disordered continuum systems, *Phys. Rev. B, 39*, 11,965–11,970, 1989.

Schwartz, L. M., J. R. Banavar, and B. I. Halperin, Biased-diffusion calculations of electrical transport in inhomogeneous continuum systems, *Phys. Rev. B, 40*, 9155–9161, 1989.

Sibson, R. H., Fluid flow accompanying faulting: field evidence and models, in *Earthquake Prediction: An International Review, Maurice Ewing Ser.*, vol. 4, edited by D. W. Simpson and P. G. Richards, pp. 593–604, AGU, Washington, D. C., 1981.

Sleep, N. H., and M. L. Blanpied, Creep, compaction and the weak rheology of major faults, *Nature, 359*, 687–692, 1992.

Sleep, N. H., and M. L. Blanpied, Ductile creep and compaction: a mechanism for transiently increasing fluid pressure in mostly sealed fault zones, *PAGEOPH, 143*, 9–40, 1994.

Sprunt, E. S., and A. Nur, Destruction of porosity through pressure solution, *Geophysics, 42*, 726–741, 1977a.

Sprunt, E. S., and A. Nur, Experimental study of the effects of stress on solution rate, *J. Geophys. Res., 82*, 3013–3022, 1977b.

Timur, A., W. B. Hempkins, and A. E. Worthington, Porosity and pressure dependence of formation resistivity factor for sandstones, *Transactions of Fourth Formation Evaluation Symposium*, Canadian Well Logging Society, Calgary, 1972.

Walder, J., and A. Nur, Porosity reduction and crustal pore pressure development, *J. Geophys. Res., 89*, 11,539–11,548, 1984.

Walsh, J. B., and W. F. Brace, The effect of pressure on porosity and the transport properties of rock, *J. Geophys. Res., 89*, 9425–9431, 1984.

Watson, E. B., and J. M. Brenan, Fluids in the lithosphere, 1, Experimentally-determined wetting characteristics of $CO_2 - H_2O$ fluids and their implications for fluid transport, host-rock physical properties, and fluid inclusion formation, *Earth Planet. Sci. Lett., 85*, 497–515, 1987.

Zhang, S., M. S. Paterson, and S. F. Cox, Porosity and permeability evolution during hot isostatic pressing of calcite aggregates, *J. Geophys. Res., 99*, 15,741–15,760, 1994.

Zhu, W., C. David, and T.-f. Wong, Network modeling of permeability evolution during cementation and hot isostatic pressing, *J. Geophys. Res.*, in press, 1995.

B. Evans, Department of Earth, Atmospheric and Planetary Sciences, Massachusetts Institute of Technology, Cambridge, MA 02138. (e-mail:brievans@athena.mit.edu)

D. Lockner, U.S. Geological Survey, Menlo Park, California 94025. (e-mail: dlockner@isdmnl.wr.usgs.gov)

(Received March 11, 1994; revised August 30, 1994; accepted October 27, 1994.)